Research Paper

Magmatic and hydrothermal zircon growth during multiple orogenic cycles in an evolving mantle wedge

Jingyi Wang [a], M. Santosh [a,b,c,*], Shanshan Li [a], Sung Won Kim [d]

[a] School of Earth Sciences and Resources, China University of Geosciences, Beijing, 29 Xueyuan Road, Beijing 100083, China
[b] Centre for Tectonics, Resources and Exploration, Department of Earth Sciences, University of Adelaide, SA 5005, Australia
[c] Department of Earth System Sciences, Yonsei University, Seoul 03722, Republic of Korea
[d] Geology Division, Korea Institute of Geoscience and Mineral Resources, Daejeon 34132, Republic of Korea

ABSTRACT

The Hongseong area of the Hongseong-Imjingang Belt in the central-western Korean Peninsula forms part of a subduction-collision system that is correlated with the Qinling-Dabie-Sulu Belt in China. Several serpentinized ultramafic bodies carrying blocks of metamorphosed mafic rocks occur in this area. Here we investigate zircon grains in serpentinites from Bibong (BB) and Wonnojeon (WNJ), and high-pressure (HP) mafic granulite from Baekdong (BD) localities based on U—Pb, REE and Lu—Hf analyses. The zircons from BD HP mafic granulite show distinct age peaks at 838 Ma, 617 Ma and 410 Ma, with minor peaks at 1867 Ma, 1326 Ma and 167 Ma. The Neoproterozoic age peaks in these rocks as well as in the serpentinites suggest subduction-related melt-fluid interaction in the mantle wedge at this time. The older zircon grains ranging in age from the Early to Middle Paleoproterozoic might represent detrital grains from the basement rocks transferred to the wedge mantle through sediment subduction. The BD HP mafic granulite shows a Middle Paleozoic age peak (Devonian; 410 Ma). The 242—245 Ma age peaks in the compiled age data of zircon grains serpentinites from BB and WNJ correspond to a major Triassic event that further added melts and fluids into the ancient mantle wedge to crystallize new zircons. In the chondrite normalized rare earth element diagram, the magmatic zircon grains from the studied rocks show LREE depletion and HREE enrichment with sharply negative Eu and Pr anomalies and positive Ce and Sm anomalies. The REE patterns of hydrothermal zircons show LREE enrichment, and relatively flat patterns with negative Eu anomaly. Zircon Hf signature from the WNJ serpentinite show negative $\varepsilon_{Hf}(t)$ (−18.5 and −23.5) values indicating an enriched mantle source with T_{DM} in the range of 1614 Ma and 1862 Ma. Zircons from the BD HP mafic granulite also show slightly negative $\varepsilon_{Hf}(t)$ (average −4.3) and T_{DM} in the range of 1365—1935 Ma. Our study provides evidence for multiple zircon growth in an evolving mantle wedge that witnessed melt and fluid interaction during different orogenic cycles.

1. Introduction

Although zircon is a rare mineral in the ultramafic mantle lithologies, melt-fluid interaction through magmatic and metasomatic processes in convergent plate margins generates both magmatic and hydrothermal zircon grains in the suprasubduction mantle wedge (e.g., Shi et al., 2008; Lei et al., 2016; Hu et al., 2017; Yang et al., 2017). Careful textural, geochemical and isotopic data can provide important insights into the nature of zircon growth through melt- and fluid-related processes during serpentinization (e.g., Hu et al., 2017; Yang et al., 2017; Li et al., 2018).

The southern part of the Hongseong—Imjingang orogenic belt (viz. Hongseong-Imjingang Belt) in the central-western Korean Peninsula has been the focus of several recent studies following the discovery of dismembered serpentinized ultramafic and HP mafic granulite blocks in the Hongseong area (e.g., Oh et al., 2005; Kim et al., 2006, 2014, 2015, 2018; Park et al., 2014a, b). These findings provided important insights into the Phanerozoic convergent tectonics in the Korean Peninsula and its eastward extension into the Central China Orogenic Belt (termed as the Qinling-Dabie-Sulu

orogenic belt) between the North and South China cratons (Fig. 1; e.g., Kim et al., 2011a, 2014b, 2018; Kwon et al., 2013; Santosh et al., 2018). Several slivers of chaotic serpentinite bodies (e.g., Baekdong, Bibong, Daehung, Singok, Gwangcheon, and Wonnojeon) also carry blocks and boudins of Neoproterozoic gneiss and alkali granites as well as Neoproterozoic and Late Paleozoic high-pressure mafic granulites (Fig. 2; Kim et al., 2011; Park et al., 2014a, b; Kim and Park, 2016). The dismembered mafic rocks occurring as irregular lenticular bodies experienced high-grade metamorphism (Kim et al., 2006, 2018; Park et al., 2014b), such as the HP mafic granulites at Bibong, Baekdong, Daepan and Sinri (Fig. 2). The serpentinite and mafic rocks has been considered as keys for tectonic correlation of the Hongseong area with the Chinese Qinling-Dabie-Sulu belt (e.g. Oh et al., 2005; Kim et al., 2006, 2018; Kwon et al.,

2013). However, the protolith and tectonic evolution of these dismembered serpentinite and mafic bodies remain controversial. For example, the Baekdong serpentinite body has been variously interpreted as hydrated upper mantle fragment below a passive margin (Seo et al., 2005), hydrated mantle section of Neo-proterozoic suprasubduction ophiolite (Oh et al., 2010, 2012) and Late Paleozoic forearc mélange (Kim et al., 2011b). A recent study on the Baekdong serpentinite, together with the Gwangcheon and Wonnojeon serpentinites, reported primary chromian spinels with compositions corresponding to forearc magma generated through partial melting during the interaction between residual mantle and melt in a suprasubduction zone environment during the Late Paleozoic (Park et al., 2014a). The Bibong HP mafic granulite has been variously interpreted as a mafic rock formed in a
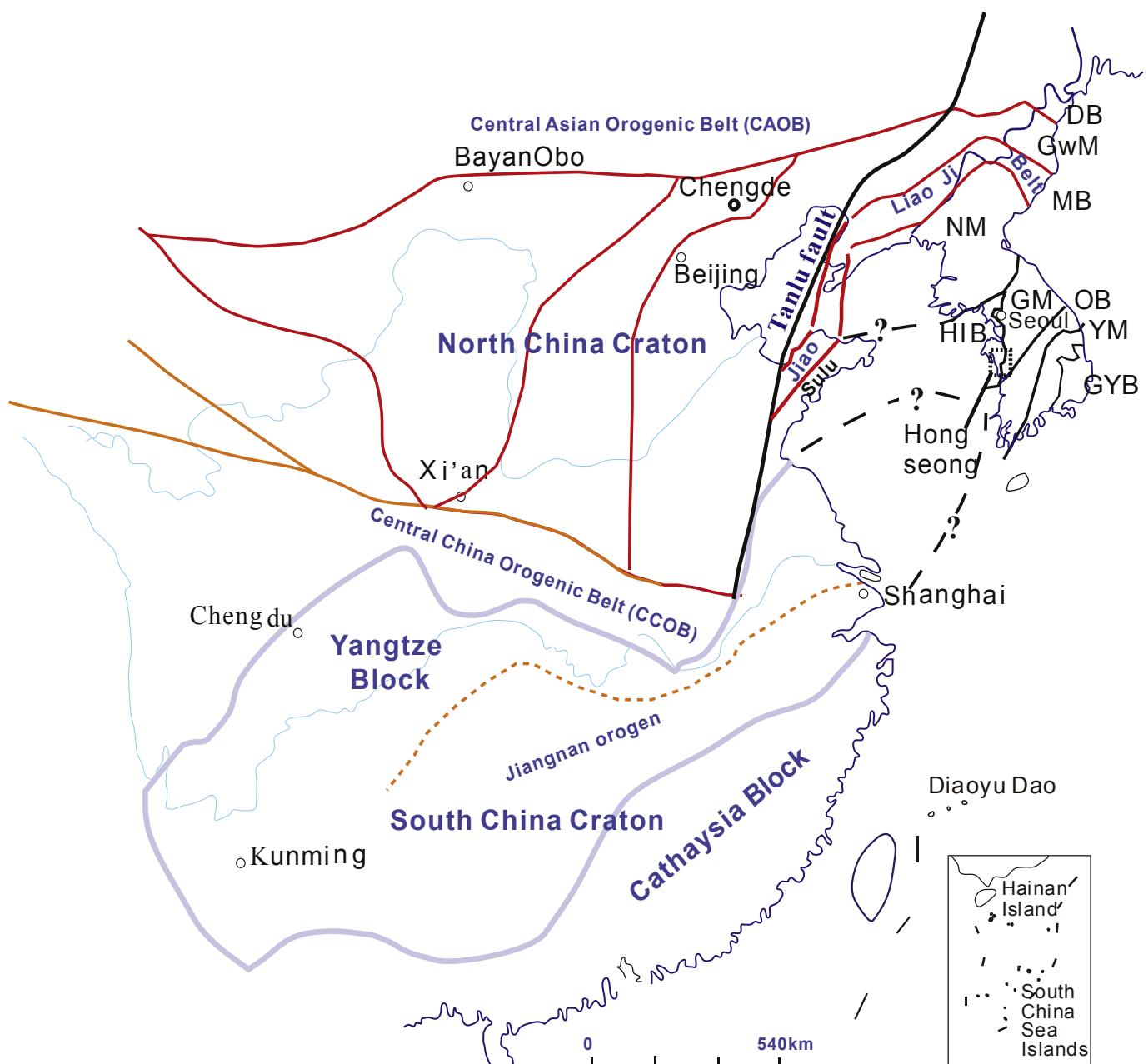

Figure 1. Simplified tectonic map of Northeast Asia showing the locations of Hongseong area. DB, Dumangang Belt; MB, Macholyong Belt; GwM, Gwanmo Massif; NM, Nangnim Massif; HIB, Hongseong–Imjingang Belt; GM, Gyeonggi Massif; OB, Okcheon Belt; YM, Yeongnam Massif; GYB, Gyeongsang Basin. Dashed lines with question mark represent inferred extension.
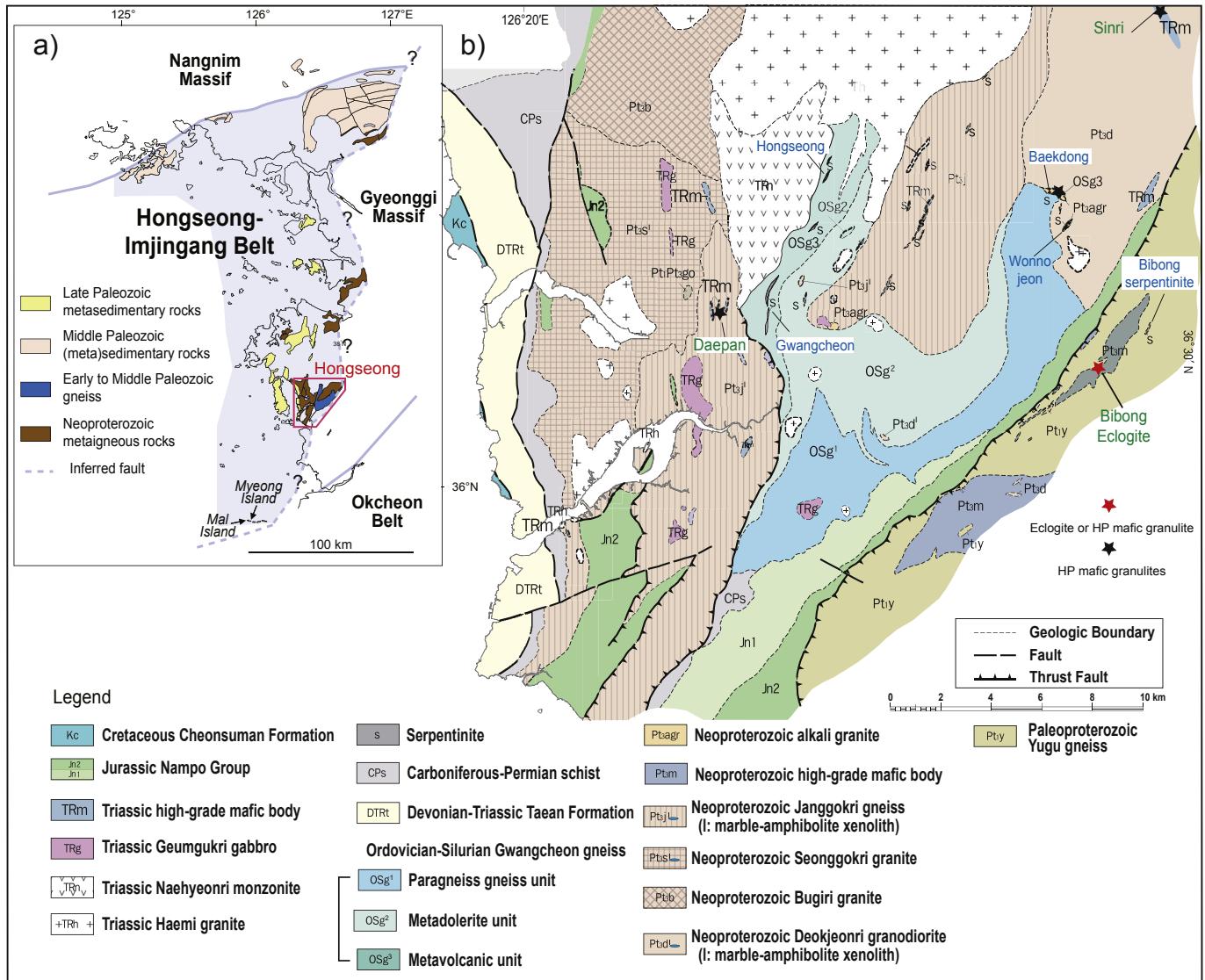
Figure 2. (a) Map showing distribution of the Hongseong–Imjingang Belt, central-western Korean Peninsula. (b) Geologic map of the Hongseong area, southern Hongseong–Imjingang Belt, showing the locations of dismembered high-grade mafic and serpentinized ultramafic bodies. The locations of Bibong, Wonnojeon and Baekdong serpentinized ultramafic bodies investigated in this study are also shown.

suprasubduction (Kim et al., 2006), an island arc (Oh et al., 2005), a backarc, or a forearc (Kwon et al., 2013) setting during the Neoproterozoic. Additionally, the two distinct Neoproterozoic (890–860 Ma) and Late Paleozoic (ca. 310 Ma; Kim et al., 2011b) protolith ages of the enclosed HP mafic granulites in the Baekdong serpentinite have stirred up controversy regarding the origin of the protolith and the tectonic implications of the dismembered serpentinite. Thus, age, Hf and trace element signatures of zircon grains from serpentinite and HP mafic granulite block in serpentinite mélanges in the Hongseong area will provide important clues on convergent plate margin processes.

In this study, we report zircon trace element analysis, LA-MC-ICPMS U–Pb dating and Lu–Hf isotope data from the serpentinites from Bibong (BB) and Wonnojeon, (WNJ) and high-pressure (HP) mafic granulite from Baekdong (BD) localities in the Hongseong-Imjingang Belt of the central-western Korean Peninsula. Compiled with the previously reported age data from dismembered serpentinite and mafic bodies in the Hongseong area, we attempt to elucidate the growth of magmatic and hydrothermal zircons during multiple subduction

events in the context of Precambrian to Phanerozoic framework of the Sino-Korean Peninsula of East Asia.

2. Geological background and sampling

The Hongseong–Imjingang Belt shows a broad N–S to NE–SW structural trend and is exposed mainly along the central-western domain of the Korean Peninsula (Fig. 2). The belt has been newly defined as a distinct tectonic province and a Phanerozoic folded belt by combining the former E–W trending Imjingang Belt and the N–S trending western margin of the Gyeonggi Massif (Figs. 1 and 2; Kim et al., 2014, 2017, 2018). Recent studies have focused on this tectonic province for gaining insights on the crustal evolution and tectonic processes in East Asia, and also for correlation with the Qinling-Dabie-Sulu Orogenic Belt which marks the collision zone between the North and South China cratons during the Permo-Triassic (ca. 245–218 Ma), as several post-collisional granitic rocks are also extensively exposed in and around the Hongseong-Imjingang Belt. The basement of the Hongseong-Imjingang Belt
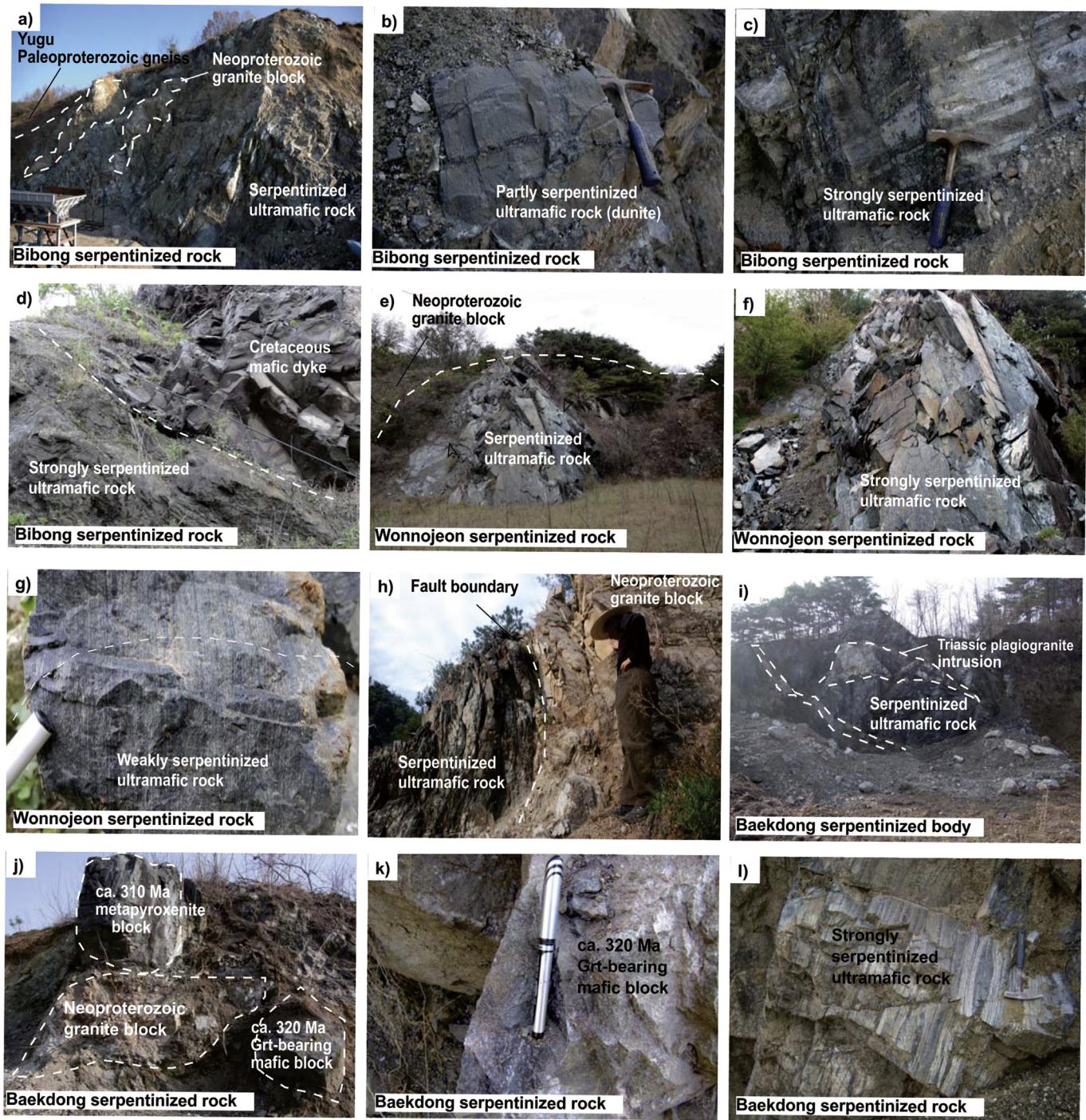
Figure 3. Outcrop photographs showing the Bibong, Wonnojeon and Baekdong serpentinized ultramafic bodies. (a)—(d) the Bibong body surrounded by the Paleoproterozoic Yugu gneiss consists of weakly to strongly serpentinized ultramafic rock. The body includes ca. 760—730 Ma Neoproterozoic alkali granite block and is intruded by ca. 110 Ma Cretaceous andesitic dyke and basaltic rock. (e)—(h) The Wonnojeon body surrounded by Neoproterozoic alkali granite, consists mostly of strongly serpentinized ultramafic rock. The boundary between the Wonnojeon body and the Neoproterozoic alkali granite shows fault contact. (i)—(l) The Baekdong body surrounded by Neoproterozoic alkali granite and composed mostly of strongly serpentinized ultramafic rock. The body includes the Carboniferous HP mafic granulite blocks and is intruded by ca. 228 Ma plagiogranite (or anorthosite).

are composed of Middle Paleoproterozoic basement rocks of the Gyeonggi Massif. The Paleozoic Gwangcheon Gneiss, Imjin System, Yeoncheon Group, Taean Formation, and the Mesozoic Nampo and Kimpo groups form the main part of the fold belt (Kim et al., 2017, 2018). However, the boundary between the Gyeonggi Massif and the Hongseong—Imjingang Belt is not well defined because most of the Neoproterozoic to Phanerozoic sedimentary sequences

deposited on the basement of the western Gyeonggi Massif are exposed along the coast or in the island areas. In addition, they are not distributed continuously, making it hard to trace them.

The Hongseong area is located in the southern part of the Hongseong-Imjingang Belt (Fig. 2a). The major rock types in this area include (1) the Neoproterozoic paragneisses and orthogneisses associated with arc-related tonalite—trondhjemite—granodiorite

(TTG) suites (Kim et al., 2008, 2013, 2014b), (2) Paleozoic paragneiss and metavolcanic and metasedimentary rocks (e.g., the Gwangcheon Gneiss and Taean Formation; Cho et al., 2010; Kim et al., 2011b, 2014a, b, 2015, 2017a, b), and (3) Mesozoic sedimentary and igneous rocks (Jeon et al., 2007; Park et al., 2009; Kim et al., 2011a). The eastern part of the Hongseong area in the Hongseong–Imjingang Belt is in contact with the ca. 1.89–1.86 Ga Paleoproterozoic Yugu gneiss in the Gyeonggi Massif (Fig. 2b). The dismembered serpentinized ultramafic bodies occur as lenticular bodies in and around the boundary between the Paleoproterozoic Yugu gneiss in the Gyeonggi Massif, and Neoproterozoic paragneisses together with orthogneisses in the Hongseong–Imjingang Belt (Fig. 2b). The other dismembered serpentinized ultramafic bodies occur in the Neoproterozoic alkali granite or along the boundary between the Neoproterozoic gneiss and the Paleozoic gneiss (Kim et al., 2011b, 2014b, 2016). The foliations of the serpentinized ultramafic rocks are concordant with overall trend of the lenticular body. Most of these ultramafic bodies are strongly serpentinized (Fig. 3), although some domains partly preserve the residual composition of dunite/lherzolite and harzburgite (Seo et al., 2005, 2013; Oh et al., 2010, 2012; Park et al., 2014a; Kim and Park, 2016). The dunite and harzburgite include olivine, orthopyroxene, clinopyroxene, chrome spinel and amphibole. The strongly

serpentinized samples consist mostly of serpentine of lizardite and chrysotile, talc, chrome spinel and Ti–Fe rich opaque minerals. Some serpentinized ultramafic bodies partly include garnet-bearing high-pressure (HP) mafic granulite as blocks (Fig. 3; Kim et al., 2011b) which are interpreted as blocks captured from depth during serpentinite protrusion. The protolith ages of the HP mafic granulite blocks are between ca. 328 Ma and 310 Ma (Kim et al., 2011b; Park et al., 2014a; Fig. 3) suggesting that the serpentinization and protrusion of this unit occurred after Carboniferous in the Hongseong area. Mineral chemistry data on the serpentinites indicate that at least a part of the serpentinite was formed in suprasubduction setting (Oh et al., 2010, 2012; Seo et al., 2013; Park et al., 2014a). The serpentinized ultramafic bodies in the Hongseong area are introduced by Triassic plagiogranite and pegmatite or Cretaceous andesitic dyke and basaltic rocks (Fig. 3; Kim and Park, 2016).

The dismembered mafic rocks in the Hyeongsan, Daeyul, Eunha, Daepan, Bibong and Siniri localities occur sporadically as lenticular bodies in the Hongseong area (Fig. 2b; Kwon et al., 2013). The retrogressed HP mafic granulite at Bibong occurs within the Paleoproterozoic Yugu gneiss (Park et al., 2014b). Those at Daepan are found within the Early to Middle Paleozoic Gwangcheon gneiss (Kim et al., 2014b, 2015; 2017a; Park et al., 2014a). At Sinri, they occur within Neoproterozoic paragneisses and orthogneisses (Kim et al., 2014b; Fig. 2b).
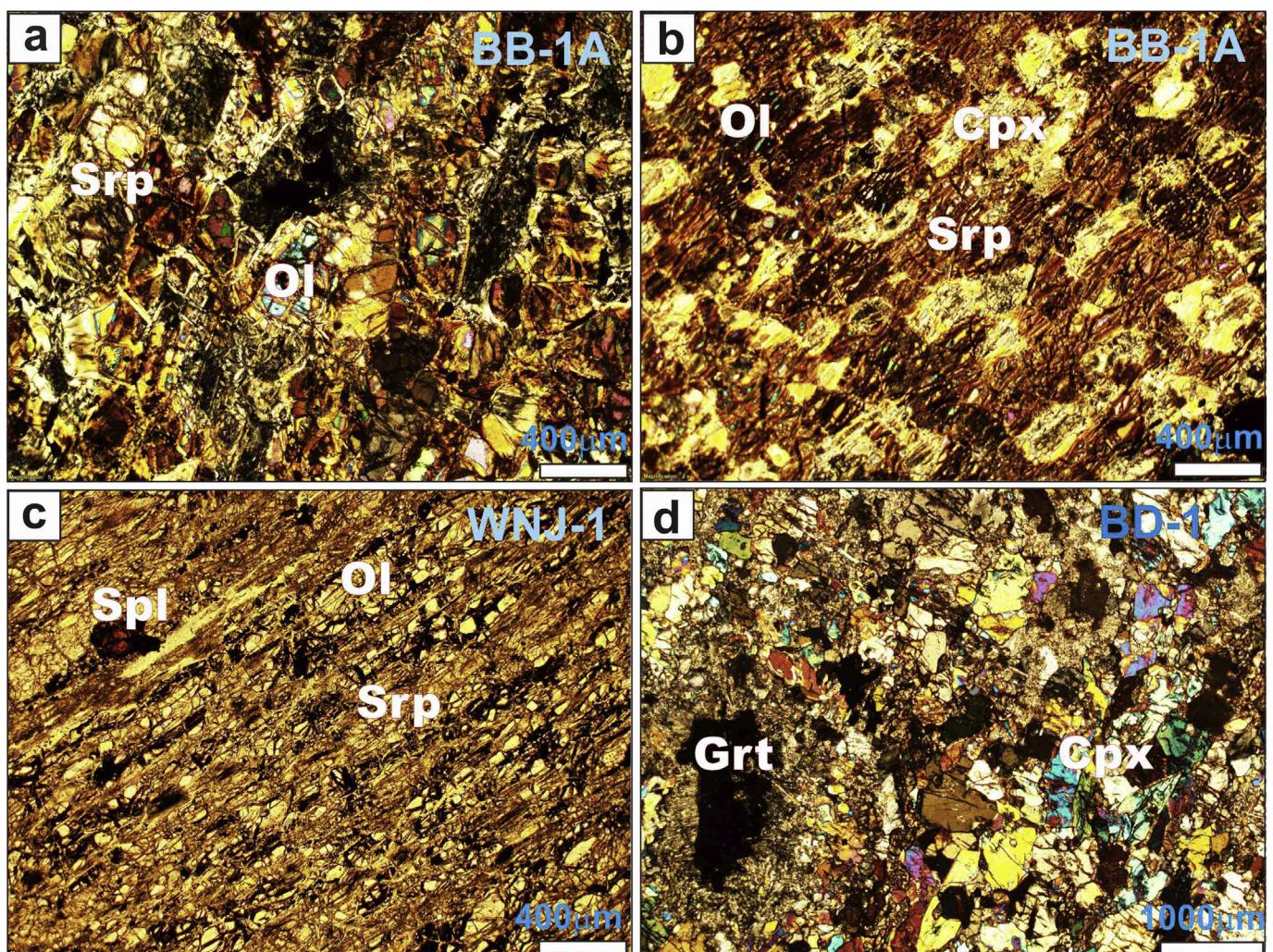
Figure 4. Thin section photomicrographs. (a) BB-1A serpentinite showing relict olivine grains within serpentinised matrix (crossed nicols). (b) BB-1A serpentinite showing tectonised fabric with relict olivine, altered clinopyroxene and serpentine (crossed nicols). (c) WNJ-1 serpentinite showing olivine, altered olivine, serpentine and chromian spinel in tectonised mosaic. (d) BD-1 HP mafic granulite showing garnet and clinopyroxene assemblage. Abbreviations: Ol–olivine; Srp–serpentine; Cpx–clinopyroxene; Spl–spinel; Grt–garnet.

Table 1
LA-ICP-MS zircon age data on serpentinites and HP mafic granulite from the Hongseong area of the southwestern Gyeonggi Massif in the central Korean Peninsula.

Spots No.	Elements content (ppm)			Isotope ratios									Age (Ma)								Concordance (%)
	Pb	Th	U	$^{207}Pb/^{206}Pb$	2σ	$^{207}Pb/^{235}U$	2σ	$^{206}Pb/^{238}U$	2σ	rho	$^{208}Pb/^{232}Th$	2σ	$^{207}Pb/^{206}Pb$	2σ	$^{207}Pb/^{235}U$	2σ	$^{206}Pb/^{238}U$	2σ	$^{208}Pb/^{232}Th$	2σ	
BB-1A serpentinite																					
BB-1A-03	82	373	434	0.0745	0.0039	1.4760	0.0572	0.1435	0.0034	0.6182	0.0401	0.0010	1056	105	921	23	865	19	794	19	94
BB-1A-04	16	21	388	0.0514	0.0047	0.2698	0.0223	0.0381	0.0011	0.3431	0.0118	0.0018	258	203	243	18	241	7	236	36	99
BB-1A-05	191	148	1168	0.0699	0.0031	1.4063	0.0374	0.1459	0.0032	0.8356	0.0410	0.0011	925	90	892	16	878	18	811	21	98
BB-1A-06	236	227	562	0.1302	0.0056	6.1050	0.1511	0.3398	0.0076	0.8988	0.0925	0.0020	2101	75	1991	22	1886	36	1787	37	90
BB-1A-07	86	47	884	0.0676	0.0032	0.8487	0.0269	0.0911	0.0021	0.7196	0.0385	0.0017	855	97	624	15	562	12	764	34	90
BB-1A-08	53	343	402	0.0643	0.0034	0.8375	0.0334	0.0944	0.0022	0.5960	0.0331	0.0008	753	111	618	18	581	13	657	16	94
BB-1A-09	29	46	187	0.0680	0.0037	1.3633	0.0569	0.1452	0.0035	0.5836	0.0406	0.0016	870	111	873	24	874	20	804	31	100
BB-1A-10	82	884	1883	0.0520	0.0026	0.2542	0.0087	0.0354	0.0008	0.6570	0.0108	0.0003	287	110	230	7	224	5	217	5	98
BB-1A-11	58	301	417	0.0654	0.0035	0.9473	0.0377	0.1050	0.0025	0.6024	0.0356	0.0009	787	110	677	20	644	15	706	18	95
BB-1A-12	26	170	277	0.0574	0.0034	0.6000	0.0279	0.0758	0.0019	0.5280	0.0243	0.0007	506	127	477	18	471	11	486	14	99
BB-1A-13	124	846	884	0.0661	0.0031	0.9051	0.0290	0.0993	0.0023	0.7160	0.0322	0.0007	810	97	655	15	610	13	640	14	93
BB-1A-14	8	230	211	0.0480	0.0053	0.1670	0.0174	0.0252	0.0008	0.2970	0.0080	0.0003	97	256	157	15	161	5	162	6	102
BB-1A-15	262	2790	1536	0.0643	0.0029	0.8756	0.0255	0.0987	0.0022	0.7783	0.0325	0.0007	753	94	639	14	607	13	646	13	95
BB-1A-16	177	1140	1072	0.0645	0.0028	1.0316	0.0286	0.1161	0.0026	0.8204	0.0346	0.0007	756	92	720	14	708	15	688	14	98
BB-1A-17	20	193	473	0.0514	0.0037	0.2516	0.0154	0.0355	0.0009	0.4235	0.0115	0.0004	259	159	228	13	225	6	231	9	99
BB-1A-18	26	195	274	0.0550	0.0032	0.5701	0.0267	0.0751	0.0018	0.5229	0.0235	0.0007	413	127	458	17	467	11	469	13	102
BB-1A-20	84	816	1894	0.0509	0.0023	0.2637	0.0082	0.0376	0.0009	0.7360	0.0114	0.0003	237	105	238	7	238	5	230	5	100
BD-1 HP mafic granulite																					
BD-1-01	8	209	257	0.0505	0.0049	0.1703	0.0152	0.0245	0.0007	0.3295	0.0077	0.0003	219	217	160	13	156	5	155	7	97
BD-1-02	73	192	152	0.1142	0.0052	5.2704	0.1618	0.3348	0.0081	0.7901	0.0967	0.0022	1867	81	1864	26	1862	39	1866	41	100
BD-1-03	57	240	462	0.0784	0.0039	1.0009	0.0355	0.0926	0.0022	0.6706	0.0365	0.0009	1157	97	704	18	571	13	725	18	81
BD-1-04	123	513	1518	0.0873	0.0040	0.8297	0.0251	0.0689	0.0016	0.7669	0.0064	0.0002	1368	87	614	14	430	10	128	5	70
BD-1-05	116	250	686	0.0828	0.0038	1.6617	0.0505	0.1456	0.0034	0.7686	0.0418	0.0011	1264	88	994	19	876	19	828	21	88
BD-1-06	54	103	455	0.0627	0.0036	0.9753	0.0439	0.1128	0.0028	0.5519	0.0344	0.0013	698	119	691	23	689	16	684	25	100
BD-1-07	152	502	848	0.0659	0.0031	1.2086	0.0384	0.1330	0.0031	0.7279	0.0397	0.0009	803	97	805	18	805	18	786	18	100
BD-1-08	40	283	467	0.0559	0.0031	0.5361	0.0229	0.0696	0.0017	0.5651	0.0208	0.0006	447	120	436	15	434	10	415	11	99
BD-1-09	7	19	67	0.0597	0.0094	0.7710	0.1168	0.0937	0.0042	0.2958	0.0311	0.0040	591	325	580	67	578	25	620	78	100
BD-1-10	181	2380	793	0.0827	0.0038	1.6528	0.0504	0.1450	0.0034	0.7604	0.0258	0.0005	1262	88	991	19	873	19	516	11	88
BD-1-11	75	137	647	0.0659	0.0031	0.9265	0.0301	0.1019	0.0024	0.7122	0.0397	0.0012	804	98	666	16	626	14	786	23	94
BD-1-12	52	173	290	0.0833	0.0039	1.6799	0.0543	0.1462	0.0034	0.7286	0.0432	0.0011	1277	91	1001	21	880	19	855	21	88
BD-1-13	108	232	687	0.0675	0.0031	1.2982	0.0386	0.1395	0.0032	0.7713	0.0440	0.0011	852	93	845	17	842	18	870	20	100
BD-1-14	41	215	534	0.0546	0.0028	0.4860	0.0183	0.0645	0.0015	0.6168	0.0188	0.0005	397	112	402	13	403	9	377	10	100
BD-1-15	41	208	543	0.0594	0.0034	0.5269	0.0241	0.0643	0.0016	0.5382	0.0306	0.0009	583	123	430	16	402	10	609	17	93
BD-1-16	60	108	576	0.0559	0.0033	0.4847	0.0226	0.0629	0.0015	0.5258	0.0314	0.0029	447	127	401	15	393	9	624	57	98
BD-1-17	40	87	341	0.0666	0.0033	0.9301	0.0327	0.1013	0.0024	0.6672	0.0316	0.0010	824	102	668	17	622	14	629	19	93
BD-1-18	102	221	886	0.0630	0.0030	0.8789	0.0287	0.1011	0.0023	0.7098	0.0298	0.0008	710	100	640	15	621	14	594	17	97
BD-1-19	22	68	209	0.0655	0.0044	0.8377	0.0471	0.0928	0.0025	0.4716	0.0343	0.0016	789	137	618	26	572	15	681	31	93
BD-1-20	89	317	686	0.0651	0.0034	1.1135	0.0433	0.1241	0.0030	0.6180	0.0362	0.0010	777	108	760	21	754	17	718	20	99
BD-1-21	171	69	2257	0.0560	0.0025	0.5409	0.0149	0.0700	0.0016	0.8077	0.0223	0.0009	453	97	439	10	436	9	446	19	99
BD-1-22	78	186	571	0.0647	0.0034	1.0374	0.0412	0.1163	0.0028	0.6061	0.0496	0.0017	764	110	723	21	709	16	979	33	98
BD-1-23	49	467	638	0.0571	0.0029	0.4672	0.0174	0.0594	0.0014	0.6232	0.0171	0.0004	493	112	389	12	372	8	343	8	96
BD-1-24	47	79	160	0.0960	0.0046	3.1282	0.1010	0.2364	0.0056	0.7362	0.0726	0.0020	1547	88	1440	25	1368	29	1417	37	95
BD-1-25	92	120	816	0.0696	0.0036	0.9771	0.0378	0.1018	0.0024	0.6192	0.0422	0.0016	918	106	692	19	625	14	836	32	90
BD-1-26	35	66	698	0.0761	0.0042	0.3819	0.0158	0.0364	0.0009	0.5840	0.0444	0.0016	1099	108	329	12	230	5	877	32	70
BD-1-27	139	65	1330	0.0659	0.0030	0.9280	0.0265	0.1021	0.0023	0.7879	0.0536	0.0019	805	93	667	14	627	13	1056	36	94
BD-1-28	106	90	387	0.0840	0.0043	2.5457	0.0966	0.2198	0.0054	0.6473	0.0650	0.0025	1292	99	1285	28	1281	29	1273	48	100
BD-1-31	64	1496	2019	0.0536	0.0028	0.1871	0.0073	0.0253	0.0006	0.5899	0.0069	0.0002	352	117	174	6	161	4	140	3	93
WNJ-1A serpentinite																					
WNJ-1A-01	24	288	483	0.0521	0.0039	0.2992	0.0198	0.0417	0.0011	0.4063	0.0130	0.0005	289	168	266	15	263	7	261	10	99
WNJ-1A-02	21	99	466	0.0524	0.0042	0.2873	0.0208	0.0398	0.0011	0.3824	0.0127	0.0008	301	180	256	16	252	7	255	16	98

Sample																					
WNJ-1A-03	59	76	91	0.1687	0.0076	11.2864	0.3402	0.4851	0.0122	0.8330	0.1301	2545	0.0034	75	2547	28	2550	53	2473	61	100
WNJ-1A-04	100	167	236	0.1120	0.0049	5.0685	0.1393	0.3282	0.0077	0.8514	0.0922	1832	0.0021	78	1831	23	1830	37	1783	39	100
WNJ-1A-05	15	93	186	0.0618	0.0054	0.5795	0.0456	0.0680	0.0020	0.3815	0.0222	668	0.0011	181	464	29	424	12	443	22	91
WNJ-1A-07	21	119	282	0.0596	0.0049	0.5545	0.0412	0.0675	0.0020	0.3904	0.0228	587	0.0011	175	448	27	421	12	455	21	94
WNJ-1A-08	196	95	365	0.1598	0.0070	10.1501	0.2858	0.4607	0.0112	0.8601	0.1241	2453	0.0043	73	2449	26	2443	49	2364	78	100
WNJ-1A-09	7	129	130	0.0565	0.0068	0.3025	0.0342	0.0388	0.0013	0.3055	0.0118	471	0.0006	257	268	27	246	8	238	12	92
WNJ-1A-10	9	146	134	0.0520	0.0056	0.3258	0.0328	0.0454	0.0015	0.3194	0.0139	287	0.0006	238	286	25	286	9	280	12	100
WNJ-1A-11	178	135	1183	0.0685	0.0030	1.3880	0.0392	0.1471	0.0034	0.8082	0.0356	882	0.0012	90	884	17	884	19	706	23	100
WNJ-1A-16	95	374	780	0.0818	0.0037	1.1268	0.0343	0.1000	0.0023	0.7625	0.0400	1240	0.0009	88	766	16	614	14	792	18	80
WNJ-1A-17	121	126	670	0.0801	0.0036	2.1245	0.0648	0.1923	0.0045	0.7670	0.0653	1200	0.0019	89	1157	21	1134	24	1279	36	98
WNJ-1A-18	70	202	398	0.0688	0.0034	1.3959	0.0489	0.1473	0.0035	0.6779	0.0497	891	0.0012	99	887	21	886	20	980	24	100
WNJ-1A-19	12	225	172	0.0533	0.0045	0.3419	0.0258	0.0465	0.0013	0.3708	0.0137	341	0.0004	184	299	20	293	8	275	9	98

3. Analytical techniques

3.1. Petrography

Polished thin sections for petrographic studies were prepared at the Peking University, China. Petrographic studies and photomicrography were carried out using an Olympus polarizing microscope with photo attachment at the China University of Geosciences Beijing, China.

3.2. Zircon separation and CL imaging

Zircon separation was carried out from crushed rock samples at the Yu'neng Geological and Mineral Separation Survey Centre, Langfang City, Hebei Province, China using gravimetric and magnetic separation techniques. The grains were handpicked under a binocular, mounted in epoxy resin discs and polished at the Beijing Geoanalysis Centre, China. The zircon grains were imaged under both transmitted and reflected light under a petrological microscope and CL imaging was done using a scanning electron microscope (JSM510) equipped with Gantan CL probe to identify internal structures and choose the target sites for U–Pb analyses.

3.3. Zircon U–Pb geochronology and REE geochemistry

Zircon U–Pb and REE analyses were carried out at the National Key Laboratory of Continental Dynamics, Northwest University, China using laser ablation inductively coupled plasma spectrometry (LA-ICP-MS) following methods described in Yuan et al. (2004). The laser spot diameter and frequency were 30 μm and 10 Hz, respectively. Zircon 91500 was employed as a standard and the standard silicate glass NIST was used to optimise the instrument. The raw data were processed using GLITTER program to calculate isotopic ratios and ages. Data were corrected for common lead, according to the method of Anderson (2002), and the ages were calculated by ISO-PLOT 4.15 software (Yuan et al., 2004). Kernel density diagrams were prepared following the methods outlined by Spencer et al. (2017). For old zircons (>1500 Ma), we computed the $^{207}Pb/^{206}Pb$ ages, whereas for younger zircons, the $^{206}Pb/^{238}U$ ages are used.

3.4. Zircon Lu–Hf isotopes

Zircon in-situ Hf isotopic analyses were carried out at the Tianjin Institute of Geology and Mineral Resources, China, by using a Neptune MC-ICP-MS equipped with a 193 nm Geolas Q Plus ArF exciplex laser ablation, with spot sizes of 50 μm. Zircon GJ-1 was used as an external standard for In-situ zircon Hf isotopic analyses. The measured $^{176}Hf/^{177}Hf$ ratios of the standard zircon GJ-1 were 0.282006 ± 24 ($n = 159$, 2σ), which is similar to the recommended $^{176}Hf/^{177}Hf$ ratio of 0.282003 ± 18 (Gerdes and Zeh, 2006).

4. Results

4.1. Petrography

The serpentinites from BB and WNJ serpentinized ultramafic bodies represent hydrated and tectonised mantle peridotites (Fig. 4a–c) with protolith composition corresponding to harzburgite or harzburgite and dunite. The major minerals are serpentinised olivine, orthopyroxene, clinopyroxene, amphibole, phlogopite, chlorite and spinel. Fractured grains of olivine form relict islands dissected by networks of serpentinite veins. The alteration assemblages include lizardite, chlorite, chrysotile, talc and magnetite. Zircon occurs as a minor accessory.
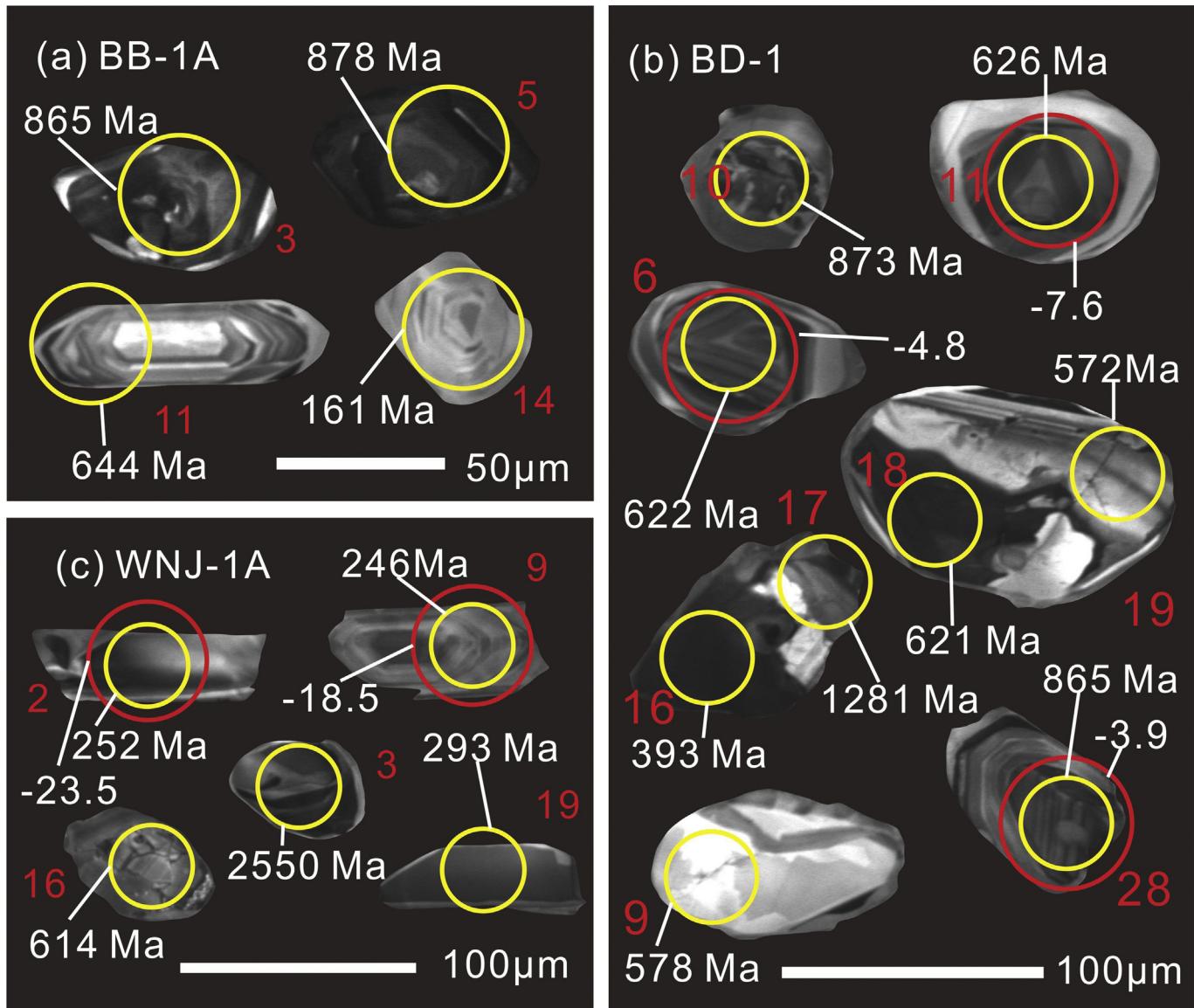
Figure 5. Representative cathodoluminescence (CL) images of zircon grains from (a) serpentinite (BB-1A), (b) HP mafic granulite (BD-1) and (c) serpentinite (WNJ-1A). Zircon U–Pb ages (Ma) and $\varepsilon_{Hf}(t)$ values are also shown. The smaller yellow circles indicate spots of LA-ICP-MS U–Pb dating, whereas the larger red circles represent locations of Hf isotopic analyses.
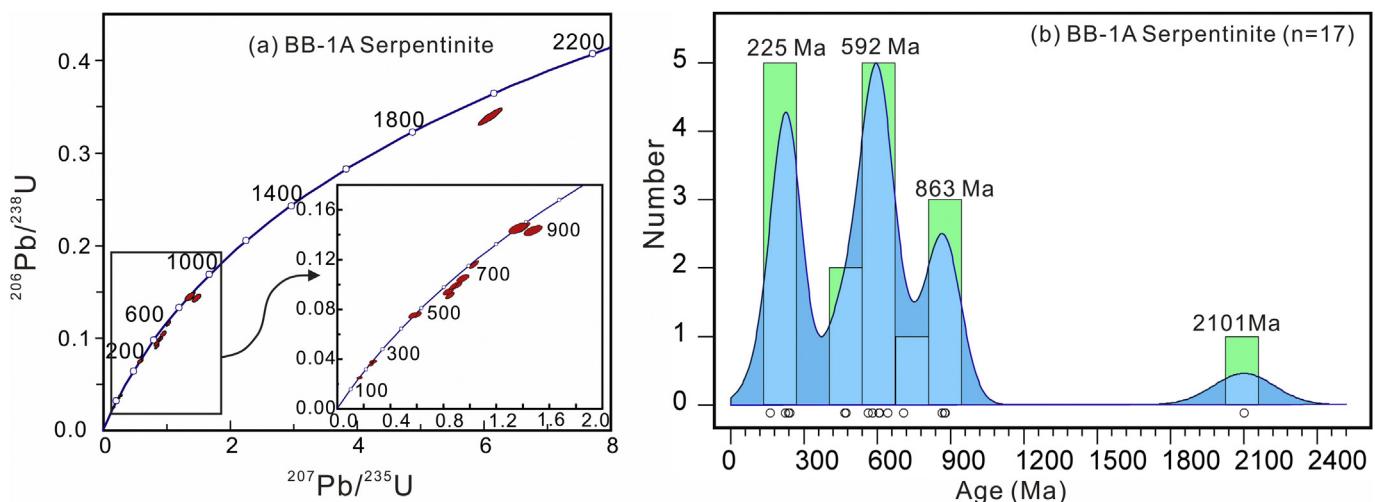

Figure 6. (a) Tera-Wasserburg concordia plots of zircon U–Pb analyses from serpentinite sample BB-1A. (b) Zircon U–Pb data using the kernel density distribution approach (Spencer et al., 2017) for the serpentinite sample BB-1A.
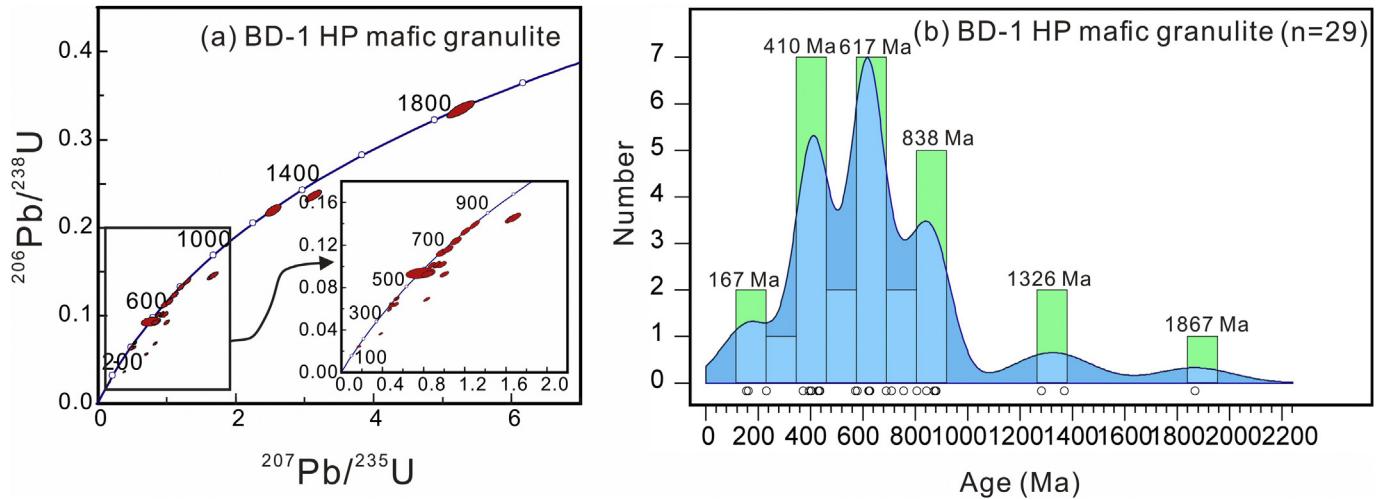
Figure 7. (a) Tera-Wasserburg concordia plots of zircon U—Pb analyses from HP mafic granulite sample BD-1. (b) Zircon U—Pb data using the kernel density distribution approach (Spencer et al., 2017) for the HP mafic granulite sample BD-1.

The garnet-bearing HP mafic granulite in BD serpentinized ultramafic body occur as disrupted blocks within serpentinite mélange. The rock is foliated with porphyroblastic grains of garnet mantled by variably thick rims of plagioclase and amphibole (Fig. 4d). The rock is dominantly composed of clinopyroxene, amphibole and plagioclase with minor biotite, epidote, quartz and titanite. Zircon occurs as a minor accessory mineral.

4.2. Zircon geochronology

Three representative samples from the Baekdong, Wonnojeon and Bibong serpentinized ultramafic bodies, comprising two serpentinites (BB-1A and WNJ-1A) and one HP garnet-bearing mafic granulite (BD-1), were selected for zircon geochronology, rare earth elements (REE) and Lu—Hf analyses using the LA-ICP-MS method. The zircon U—Pb data and REE contents are given in Table 1 and Supplementary Table 1, respectively. Representative cathodoluminescence (CL) images, age data concordia diagrams and rare earth element patterns are given in Figs. 5—9. The zircon

characteristics and age results from individual samples are briefly described below.

4.2.1. Zircon morphology
4.2.1.1. Serpentinite BB-1A. The zircon grains from this sample range in length from 30 μm to 140 μm, with length: width ratio in the range of 1:1 to 3.5:1. Most grains are colorless or light-brown to dark brown, transparent to translucent and occur as irregular subhedral to anhedral prisms. They show prismatic to sub-rounded and sometimes elliptical or elongate morphology. Needle-like apatite inclusions also can be observed in some grains. The CL images (Fig. 5a) show typical magmatic zoning textures. Few grains display core-rim texture. The cores mostly show clear oscillatory zoning, with some displaying patchy zoning or sector zoning, and are surrounded by a dark rim of less than 15 μm in width.

4.2.1.2. Serpentinite WNJ-1A. The zircon grains from serpentinite (WNJ-1A) are transparent to translucent and light dark brownish
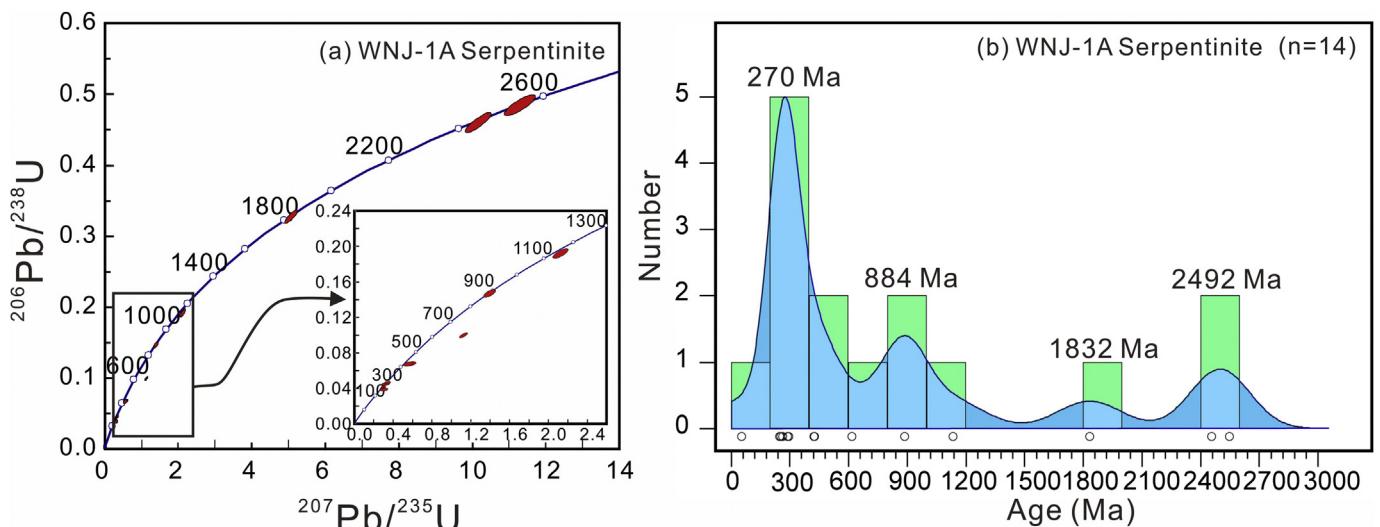

Figure 8. (a) Tera-Wasserburg concordia plots of zircon U—Pb analyses from serpentinite sample WNJ-1A. (b) Zircon U—Pb data using the kernel density distribution approach (Spencer et al., 2017) for the serpentinite sample WNJ-1A.
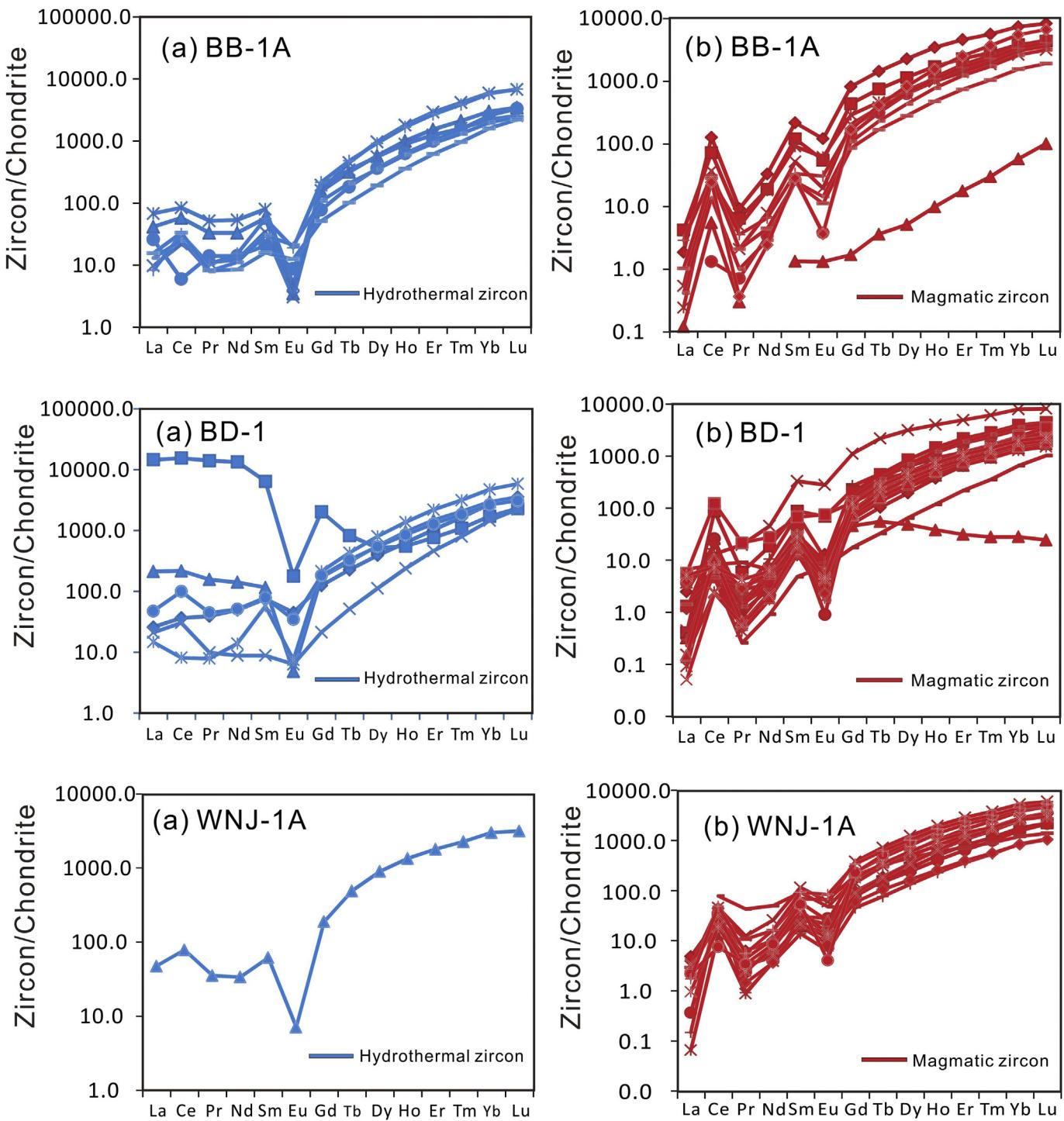
Figure 9. Chondrite-normalized REE diagrams of zircons in sample BB-1A, BD-1, and WNJ-1A. (a) Hydrothermal zircon grains (b) magmatic zircon grains. Chondrite values are after Sun and McDonough (1989).

color, with a size range of 50—100 μm and aspect ratios of 2:1 to 1:1 (Fig. 5c). Most grains are small, and euhedral to subhedral. A few of the grains are partly rounded and structureless, whereas the majority of zircon grains show banded zoning with widely separated zones. Some grains displaying core-rim texture with thin rims.

4.2.1.3. HP garnet-bearing mafic granulite BD-1. Zircons from the HP garnet-bearing mafic granulite sample (BD-1) from

Baekdong are mostly colorless or light brown. They show long elliptical or rounded morphology with length varying from 50 μm to 150 μm and aspect ratios of 2:1 to 1:1. In CL images (Fig. 5b), the grains show subhedral to anhedral shape, and core-rim textures with the cores showing oscillatory or banded zoning, and surrounded by thin and bright metamorphic rims. The internal textures are much clear and some grains show mineral/fluid inclusions. Some zircons display patchy or banded zoning.

Table 2
Zircon Lu–Hf data on serpentinites and HP mafic granulite from the Hongseong area of the southwestern Gyeonggi Massif in the central Korean Peninsula.

Spots No.	Age (Ma)	2σ	^{176}Yb/^{177}Hf	2σ	^{176}Lu/^{177}Hf	2σ	^{176}Hf/^{177}Hf	2σ	^{176}Hf/^{177}Hf$_i$	$\varepsilon_{Hf}(0)$	$\varepsilon_{Hf}(t)$	T_{DM} (Ma)	T_{DM}^c (Ma)	$f_{Lu/Hf}$
BD-1-06	689	16	0.035035	0.000156	0.000704	0.000002	0.282215	0.000014	0.282206	−19.6883	−4.83342	1451.979	2426.751	−0.97879
BD-1-11	626	14	0.028858	0.000166	0.000653	0.000005	0.282176	0.000015	0.282168	−21.082	−7.57571	1504.483	2629.546	−0.98034
BD-1-20	754	17	0.054724	0.000749	0.001263	0.000012	0.282293	0.000018	0.282275	−16.9558	−0.96306	1364.885	2124.776	−0.96196
BD-1-28	1281	29	0.052628	0.001445	0.00153	0.000042	0.281895	0.000025	0.281858	−31.002	−3.93354	1934.693	2737.333	−0.95393
WNJ-1A-2	252	7	0.057887	0.001501	0.001897	0.000051	0.28196	0.000560	0.281951	−28.7195	−23.5176	1862.329	3803.921	−0.94286
WNJ-1A-9	246	8	0.025975	0.000244	0.000806	0.000007	0.282101	0.000022	0.282098	−23.7202	−18.4622	1613.873	3353.075	−0.97573

$\varepsilon_{Hf}(0) = ((^{176}Hf/^{177}Hf)_S/(^{176}Hf/^{177}Hf)_{CHUR,0} - 1) \times 10,000$;

† $\varepsilon_{Hf}(t) = ((^{176}Hf/^{177}Hf)_S - (^{176}Lu/^{177}Hf)_S \times (e^{\lambda t} - 1))/((^{176}Hf/^{177}Hf)_{CHUR,0} - (^{176}Lu/^{177}Hf)_{CHUR} \times (e^{\lambda t} - 1)) - 1) \times 10,000$;

Single-stage depleted mantle model age: T_{DM} (Ma) $= 1/\lambda \times Ln(1 + ((^{176}Hf/^{177}Hf)_S - (^{176}Hf/^{177}Hf)_{DM})/((^{176}Lu/^{177}Hf)_S - (^{176}Lu/^{177}Hf)_{DM}))$;

Two-stage depleted mantle model age: 2s T_{DM} (Ma) $= T_{DM1} - (T_{DM1} - t) \times ((^{176}Lu/^{177}Hf)_{cc}/(^{176}Lu/^{177}Hf)_{CHUR} - (^{176}Lu/^{177}Hf)_S/(^{176}Lu/^{177}Hf)_{CHUR})/((^{176}Lu/^{177}Hf)_{cc}/$
$(^{176}Lu/^{177}Hf)_{CHUR} - (^{176}Lu/^{177}Hf)_{DM}/(^{176}Lu/^{177}Hf)_{CHUR}) = 1/\lambda \times Ln(1 + ((^{176}Hf/^{177}Hf)_{S,t} - (^{176}Hf/^{177}Hf)_{DM,t})/((^{176}Lu/^{177}Hf)_{cc} - (^{176}Lu/^{177}Hf)_{DM})) + t$;

$f_{Lu/Hf} = (^{176}Lu/^{177}Hf)_S/(^{176}Lu/^{177}Hf)_{CHUR} - 1$; t = crystallization time of zircon (in Ma), $\lambda = 1.865 \times 10^{-11}$ year^{-1} (Scherer et al., 2001); $(^{176}Lu/^{177}Hf)_{cc} = 0.015$, $(^{176}Lu/^{177}Hf)_{DM} = 0.0384$, $(^{176}Hf/^{177}Hf)_{DM} = 0.28325$ (Griffin et al., 2002); $(^{176}Lu/^{177}Hf)_{CHUR} = 0.0332$, $(^{176}Hf/^{177}Hf)_{CHUR,0} = 0.282772$ (Blichert-Toft and Albarde, 1997); $(^{176}Lu/^{177}Hf)_S$ and $(^{176}Hf/^{177}Hf)_S$ are measured values of samples.

4.2.2. U–Pb data

BB-1A. A total of 17 spots from 17 zircon grains from the serpentinite (sample BB-1A) were analyzed. The results show Th and U contents and Th/U ratios in the range of 20.99–2790.2 ppm, 186.94–1893.65 ppm, and 0.05–1.82, respectively (Table 1). The grains show spot ages or age peaks at 225 Ma, 592 Ma, 863 Ma and 2101 Ma (Fig. 6). Some younger age spots also occur (Table 1).

BD-1. Twenty nine spots were analyzed from 27 zircon grains from the HP garnet-bearing mafic granulite (sample BD-1) and the results show Th and U contents and Th/U ratios in the range of 18.54–1495.94 ppm, 186.94–1893.65 ppm, and 0.03–1.27 (Table 1). The spot ages or age peaks show 167 Ma, 410 Ma, 617 Ma, 838 Ma, 1326 Ma and 1867 Ma (Fig. 7).

WNJ-1A. A total of 14 analyses were done on the different domains from 14 zircon grains. The Th and U contents range from 76.3–390.56 ppm and 90.57–1182.52 ppm respectively with Th/U ratios ranging from 0.11 to 1.31. Fourteen data define two distinct age groups (Fig. 8, Table 1). The ^{206}Pb/^{238}U ages of the first group range from 246 Ma to 1134 Ma. The second group of three spots show Paleoproterozoic ages of 1830 Ma, 2443 Ma and 2550 Ma. Zircon grains with ^{206}Pb/^{238}U spot ages or age peaks are also observed at 270 Ma, and 884 Ma (Fig. 8).

4.3. Zircon rare earth elements

The chondrite-normalized zircon rare earth element (REE) diagrams (Sun and McDonough, 1989) are shown in Fig. 9 (see also Supplementary Table 1). Based on the REE patterns, the zircons in the studied rocks can be grouped into magmatic and hydrothermal. The magmatic grains generally display LREE depletion and HREE enrichment, with clear negative Eu and Pr anomalies and positive Ce and Sm anomalies (Fig. 9) which are typical features of igneous zircon (Hoskin and Schaltegger, 2003). The negative Pr-anomaly and Eu-anomaly are generally considered as indicators of zircons crystallized through melt-peridotite interaction (Liu et al., 2010).

The REE patterns of hydrothermal zircons in the studied rocks are markedly different from those of the magmatic grains particularly with regard to their prominent LREE enrichment, minor or no Ce and Sm anomalies, and absence of any distinct negative Pr anomaly. The negative Eu anomaly shown by these grains is typical of hydrothermal zircons. The features observed are consistent with zircon crystallization through melt-percolation, melt-peridotite interaction and hydration within a mantle wedge (Hu et al., 2017; Yang et al., 2017).

4.4. Zircon Lu–Hf isotopes

Lu–Hf isotope were analyzed in the same or adjacent domains of the zircon grains where U–Pb age data were obtained. The results of the Lu–Hf isotope analyses are given in Table 2, and plotted in Fig. 10 and the data from individual samples are briefly discussed below. Lu–Hf analyses were performed only on few zircon grains from the WNJ-1A serpentinite and BD-1 HP garnet-bearing mafic granulite because zircon is either small or rare in these rocks. No grains were analysed from BB-1A serpentinite because of too few grains and their small size.

The two grains from WNJ-1A serpentine show initial ^{176}Hf/^{177}Hf values of 0.281960 and 0.282101, with $\varepsilon_{Hf}(t)$ values in the range of −23.5 to −18.5 (Table 2). These Permo-Triassic (252–246 Ma) grains show T_{DM} of 1614 Ma and 1862 Ma suggesting Paleoproterozoic sources. Four zircon grains from BD-1 HP garnet-bearing mafic granulite show initial ^{176}Hf/^{177}Hf values in the range of 0.281895–0.282293, with $\varepsilon_{Hf}(t)$ values in the range of −7.6 to −1.0 (Table 2). These Meso-to Neoproterozoic grains (626–1281 Ma) show T_{DM} of 1365–1935 Ma suggesting mixed Paleo and Mesoproterozoic sources.
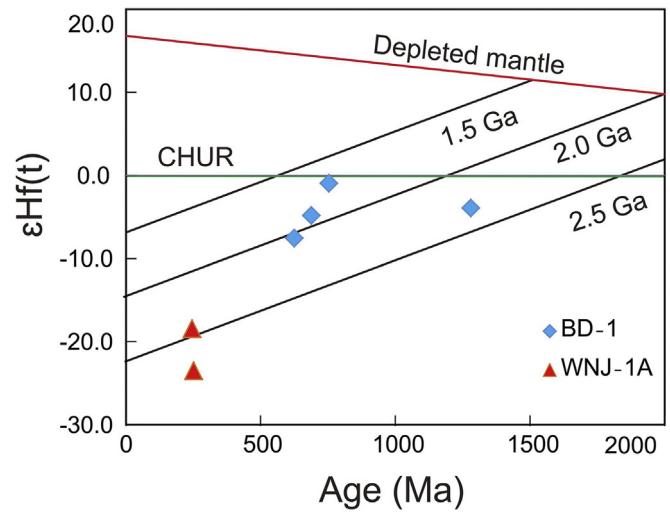

Figure 10. Zircon Hf isotopic evolution diagram from BD-1 HP mafic granulite and WNJ-1A serpentinite, CHUR-chondritic uniform reservoir. The corresponding lines of crustal extraction are calculated by using the ^{176}Lu/^{177}Hf ratio of 0.015 for the average continental crust (Griffin et al., 2002).

5. Discussion

This study focuses on zircon characteristics of representative serpentinite samples (BB-1A, WNJ-1A) and HP garnet-bearing mafic granulite (BD-1) from the Hongseong area of the central-western Korean Peninsula based on U–Pb, REE and Lu–Hf analyses.

Zircon grains in these rocks show a wide range of ages. Those from the HP garnet-bearing mafic granulite sample BD-1 yield ages in the range of 161–2101 Ma. The age data histograms and kernel density plots of zircon from HP mafic granulite (BD-1; Fig. 7) show distinct age peaks at 838 Ma, 617 Ma and 410 Ma, with minor peaks at 1867 Ma, 1326 Ma and 167 Ma. The 410 Ma age is well correlated with that reported from the surrounding Gwangcheon Gneiss (see Fig. 2). The BD HP garnet-bearing mafic granulite shows Middle Paleozoic age peak (Devonian; 410 Ma).

Zircon grains from the serpentinites (BB-1A, WNJ-1A) also belong to multiple population with the oldest grains at 2492 Ma, 2101 Ma and 1832 Ma, which are similar to those in the basement rocks in this area (Santosh et al., 2018). Younger population shows spot or peak ages at 270 Ma or 225 Ma. In the case of serpentinites from the two localities we show compiled age data diagrams in Fig. 11 where we have also included the data from a previous study (Kim and Park, 2016) from the same locations where two major peaks are seen at ca. 242–245 Ma and 698–735 Ma. These age peaks in the compiled data are slightly different from the 225–270 Ma and 863–884 Ma peaks for the individual localities obtained in this study (Figs. 6 and 8) because the published ages in Kim and Park (2016) included larger spread in ages. The Middle Neoproterozoic age peaks are common in all the rocks, suggesting subduction-related melt-fluid interaction in the mantle wedge at this time. The older zircon grains ranging in age from Early to Middle Paleoproterozoic might represent detrital grains from the basement rocks transferred to the wedge mantle through sediment subduction. The prominent 242–245 Ma age peaks in the compiled age data of zircon grains serpentinites from the two localities correspond to a major Triassic event that further added melts and fluids into the ancient mantle wedge to crystallize new zircons.

In the chondrite normalized rare earth element diagram, the magmatic zircon grains from the studied rocks show LREE depletion and HREE enrichment with clear negative Eu and Pr anomalies and positive Ce and Sm anomalies (Fig. 9) together with negative Pr and Eu anomalies. The REE patterns of hydrothermal zircons show distinctly different patterns with LREE enrichment, and relatively flat patterns with only Eu showing negative anomaly. Zircon Lu–Hf data from the serpentinite sample (WNJ1A) show $\varepsilon_{Hf}(t)$ values of −18.5 and −23.5 and Hf depleted model ages of 1614 Ma and 1862 Ma suggesting Paleoproterozoic sources, when calculated by U–Pb ages of 252 Ma and 246 Ma. Zircons from the HP garnet-bearing mafic granulite sample (BD-1) show $\varepsilon_{Hf}(t)$ values of −7.6 to −1 with model ages of 1365–1935 Ma, when calculated by U–Pb ages of 626–1281 Ma.

Based on the REE patterns, the zircon grains in the studied rocks can be divided into magmatic group and hydrothermal group. Zircon grains of magmatic group are characterized by high and variable REE contents, with a positive Ce anomaly, and negative Eu anomaly. The zircon grains of hydrothermal group show flat LREE contents, particularly marked enrichment in Sm, together with low $(Sm/La)_N$ and Ce/Ce^* values are compatible with the features of hydrothermal zircon (Hoskin, 2005). The zircon grains of hydrothermal group dominantly fall within the field of hydrothermal zircon in the $(Sm/La)_N$ vs. La plots (Fig. 12a) as well as Ce/Ce^* vs. $(Sm/La)_N$ plots (Fig. 12b). A compilation of age data histogram of all the age data from the hydrothermal group is also shown as inset in Fig. 12c, where the major peaks are at 193 Ma, 574 Ma, 871 Ma and 2101 Ma. Half of the zircon population
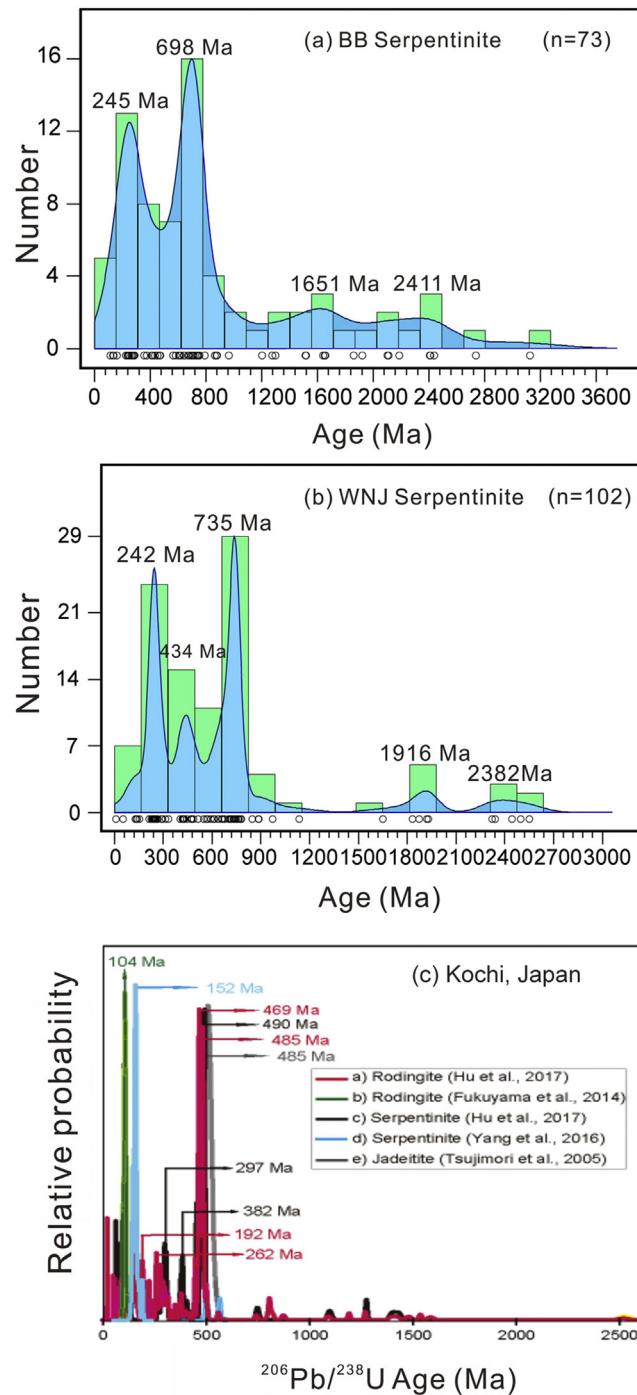

Figure 11. Compiled zircon U–Pb ages using the kernel density distribution approach (Spencer et al., 2017) for serpentinites from BB (a) and WNJ (b). The data include those from this study as well as from Kim and Park (2016). (c) Compiled zircon age data on serpentinites, rodingites and jadeitites from Kochi, SW Japan (after Hu et al., 2017, compiling data from Tsujimori et al., 2005; Fukuyama et al., 2014; Yang et al., 2016).

from the studied samples fall within the magmatic field. Several grains fall in the transitional area between magmatic and hydrothermal zircon in the Ce/Ce^* vs. $(Sm/La)_N$ plots (Fig. 12b) and in the $(Sm/La)_N$ vs. La plots (Fig. 12a).

Several previous studies have documented magmatic and hydrothermal zircon growth through melt and fluid infiltration (e.g., Tsujimori et al., 2005; Shi et al., 2008; Tsutsumi et al., 2010; Fukuyama et al., 2014; Lei et al., 2016). In a recent study, Yang
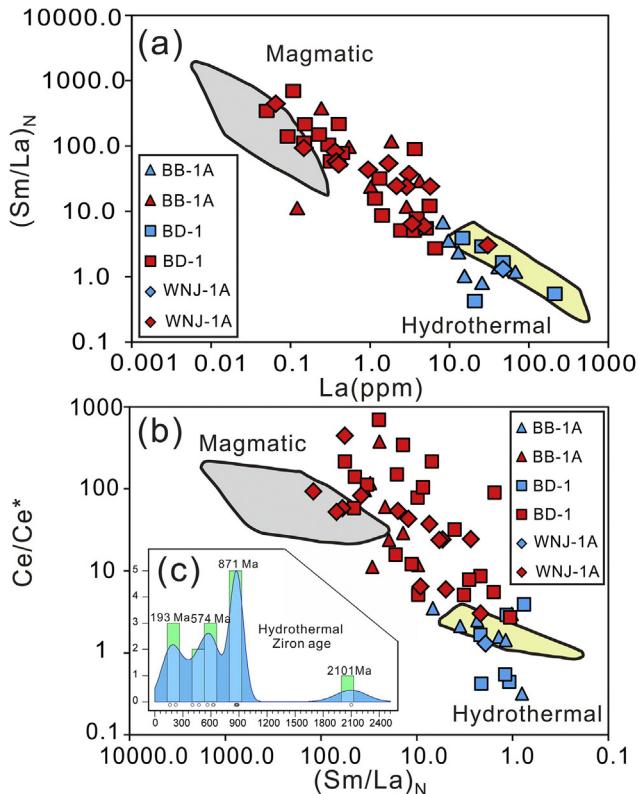
Figure 12. Discrimination plots for magmatic and hydrothermal zircon grains. (a) La–(Sm/La)$_N$, (b) (Sm/La)$_N$–Ce/Ce*, (c) all the hydrothermal zircon U–Pb data in this study using the kernel density distribution approach (Spencer et al., 2017). Grey shaded area representing magmatic field and yellow representing hydrothermal field are from Hoskin (2005). The data indicate transition from magmatic to hydrothermal zircons.

et al. (2017) traced multiple magmatism in a suprasubduction zone mantle wedge through the analysis of zircon grains from a composite mafic-ultramafic complex in Gaositai, North China Craton. The serpentinites in this complex trace the history of a long-lived and replenished ancient sub-continental lithospheric mantle and carry zircon grains from the Paleoproterozoic basement, together with newly crystallized Neoproterozoic and Paleozoic to Mesozoic grains, suggesting continuous mantle metasomatism through melts and fluids associated with prolonged subduction. Multiple zircon growth in this evolving metasomatized suprasubduction zone mantle wedge was correlated to tectonics associated with the subduction regime of the Paleo-Asian Ocean.

In another study, Hu et al. (2017) investigated zircon grains in serpentinites, pyroxenites and rodingites from Kochi along the active convergent margin in Southwest Japan. The zircon grains in these rocks show major age peaks at 485 Ma and 469 Ma, marking the timing of formation of the protoliths. The wide range of minor age peaks including those at 152 Ma and 104 Ma were correlated to continuous fluid- and melt-induced mantle metasomatism associated with subduction of the Pacific plate (Fig. 11c). The REE patterns of zircons display distinct negative Eu-anomaly, particularly in the case of hydrothermal zircons. The $\varepsilon_{Hf}(t)$ values of the zircons grains are generally positive (2–18) suggesting an isotopically primitive source (Hu et al., 2017). The tectonic evolution of serpentinites from the Hongseong area are similar to those of Kochi in SW Japan and suggests melt and fluid infiltration processes the long-lived mantle wedge which witnessed prolonged and multiple subduction systems.

6. Conclusions

Our study on zircon grains from serpentinites and high pressure mafic granulite from the Hongseong area in the central-western Korean Peninsula leads to the following salient conclusions.

(1) The few older zircon grains ranging in age from the Early to Middle Paleoproterozoic occurring in these rocks might represent detrital grains from the basement transferred to the wedge mantle through sediment subduction in an active convergent margin.
(2) The common Neoproterozoic age peaks are correlated with subduction-related melt-fluid interaction in the mantle wedge at this time.
(3) The more prominent Middle Paleozoic (Silurian 434 Ma) and the Triassic (242–245 Ma) age peaks in compiled age data Kernel density plots correspond to Phanerozoic subduction events that added further melts and fluids into the ancient mantle wedge.
(4) Both magmatic and hydrothermal zircon grains are identified. The magmatic grains display LREE depletion and HREE enrichment with negative Eu and Pr anomalies and positive Ce and Sm anomalies. The hydrothermal zircons show LREE enrichment, and relatively flat patterns with negative Eu anomaly. The negative $\varepsilon_{Hf}(t)$ (−18.5 and −23.5) values indicate an enriched mantle source.
(5) Our data are comparable to multiple zircon growth from active convergent margin mantle wedge such as in Kochi, SW Japan, and suggest zircon growth through melt and fluid interaction during different orogenic cycles.

Acknowledgments

Appendix A. Supplementary data

Supplementary data related to this article can be found at https://doi.org/10.1016/j.gsf.2018.07.003.

References

Anderson, T., 2002. Correction of common Pb in U–Pb analyses that do not report [204]Pb. Chemical Geology 192, 59–79.

Blichert-Toft, J., Albarede, F., 1997. The Lu-Hf isotope geochemistry of chondrites and the evolution of the mantle-crust system. Earth and Planetary Science Letters 148, 243–258.

Cho, M., Na, J., Yi, K., 2010. SHRIMP U–Pb ages of detrital zircons in metasandstones of the Taean Formation, western Gyeonggi massif, Korea: tectonic implications. Geoscience Journal 14, 99–109.

Fukuyama, M., Ogasawara, M., Dunkley, D.J., Wang, K.L., Lee, D.C., Hokada, T., Maki, K., Hirata, T., Kon, Y., 2014. The formation of rodingite in the Nagasaki metamorphic rocks at Nomo Peninsula, Kyushu, Japan – zircon U–Pb and Hf isotopes and trace element evidence. Island Arc 23, 281–298.

Gerdes, A., Zeh, A., 2006. Combined U-Pb and Hf isotope LA-(MC-)ICP-MS analyses of detrital zircons: comparison with SHRIMP and new constraints for the provenance and age of an Armorican metasediment in Central Germany. Earth and Planetary Science Letters 249, 47–61.

Griffin, W.L., Wang, X., Jackson, S.E., Pearson, N.J., O'Reilly, S.Y., Xu, X., Zhou, X., 2002. Zircon chemistry and magma mixing, SE China: in-situ analysis of Hf isotopes. Tonglu and Pingtan igneous complexes. Lithos 61, 237–269.

Hoskin, P.W.O., 2005. Trace-element composition of hydrothermal zircon and the alteration of Hadean zircon from the Jack Hills, Australia. Geochimica et Cosmochimica Acta 69 (3), 637–648.

Hoskin, P.W., Schaltegger, U., 2003. The composition of zircon and igneous and metamorphic petrogenesis. Reviews in Mineralogy and Geochemistry 53 (1), 27–62.

Hu, C.N., Santosh, M., Yang, Q.Y., Kim, S.W., Nakagawa, M., Maruyama, S., 2017. Magmatic and metasomatic imprints in a long-lasting subduction zone: evidence from zircon in rodingite and serpentinite of Kochi, SW Japan. Lithos 274, 349–362.

Jeon, H., Cho, M., Kim, H., Horie, K., Hidaka, H., 2007. Early Archean to middle Jurassic evolution of the Korean Peninsula and its correlation with Chinese cratons: SHRIMP U-Pb zircon age constraints. The Journal of Geology 115, 525–539.

Kim, S.W., Cho, D.-L., Lee, S.-B., Kwon, S., Park, S.-I., Santosh, M., Kee, W.-S., 2018. Mesoproterozoic magmatic suites from the central-western Korean Peninsula: imprints of columbia disruption in East Asia. Precambrian Research 306, 155–173.

Kim, S.W., Kee, W.-S., Lee, S.R., Santosh, M., Kwon, S., 2013. Neoproterozoic plutonic rocks from the western Gyeonggi massif, South Korea: implications for the amalgamation and break-up of the Rodinia supercontinent. Precambrian Research 227, 349–367.

Kim, S.W., Kwon, S., Park, S.-I., Yi, K., Santosh, M., 2017a. Early to Middle Paleozoic tectonometamorphic evolution of the Hongseong area, central western Korean Peninsula: tectonic implications. Gondwana Research 47, 308–322.

Kim, S.W., Kwon, S., Park, S.-I., Yi, K., Santosh, M., Ryu, I.-C., 2015. Early to Middle Paleozoic arc magmatism in the Korean Peninsula: constraints from zircon geochronology and geochemistry. Journal of Asian Earth Sciences 113, 866–882.

Kim, S.W., Kwon, S., Santosh, M., Cho, D.L., Ryu, I.-C., 2014a. Detrital zircon U–Pb geochronology and tectonic implications of the Paleozoic sequences in western South Korea. Journal of Asian Earth Sciences 95, 217–227.

Kim, S.W., Kwon, S., Santosh, M., Williams, I.S., Yi, K., 2011a. A Paleozoic subduction complex in Korea: SHRIMP zircon U–Pb ages and tectonic implications. Gondwana Research 20, 890–903.

Kim, S.W., Park, S.-I., 2016. Geochronological and geotectonic implications of the serpentinite bodies in the Hongseong area, central-western Korean Peninsula. Economic and Environmental Geology 49, 249–267.

Kim, S.W., Park, S.-I., Jang, Y., Kwon, S., Kim, S.J., Santosh, M., 2017b. Tracking Paleozoic evolution of the South Korean Peninsula from detrital zircon records: implications for the tectonic history of East Asia. Gondwana Research 50, 195–215.

Kim, S.W., Park, S.-I., Ko, K., Lee, H.-J., Koh, H.J., Kihm, Y.H., Lee, S.R., 2014b. 1:100,000 Tectonostratigraphic Map of the Hongseong Area, Map 1: Solid Geology Interpretation. Korea Institution of Geoscience and Mineral Resources.

Kim, S.W., Oh, C.W., Williams, I.S., Rubbato, D., Ryu, I.-C., Rajesh, V.J., Kim, C.-B., Guo, J., Zhai, M., 2006. Phanerozoic high-pressure eclogite and intermediate-pressure granulite facies metamorphism in the Gyeonggi block, South Korea: implications for the eastward extension of the Dabie-Sulu continental collision zone. Lithos 92, 357–377.

Kim, S.W., Santosh, M., Park, N., Kwon, S., 2011b. Forearc serpentinite mélange from the Hongseong suture, South Korea. Gondwana Research 20, 852–864.

Kim, S.W., Williams, I.S., Kwon, S., Oh, C.W., 2008. SHRIMP zircon geochronology and geochemical characteristics of metaplutonic rocks from the south-western Gyeonggi block, Korea: implications for Paleoproterozoic to Mesozoic tectonic links between the Korean Peninsula and eastern China. Precambrian Research 162, 475–497.

Kwon, S., Kim, S.W., Santosh, M., 2013. Multiple generations of mafic–ultramafic rocks from the Hongseong suture zone, western South Korea: implications for the geodynamic evolution of NE Asia. Lithos 160–161, 68–83.

Lei, W., Shi, G., Santosh, M., Ng, Y., Liu, Y., Wang, J., Xie, G., Ju, Y., 2016. Trace element features of hydrothermal and inherited igneous zircon grains in mantle wedge environment: a case study from the Myanmar jadeitite. Lithos 266–267, 16–17.

Li, S.S., Keerthy, S., Santosh, M., Singh, S.P., Deering, C.D., Satyanarayanan, M., Praveen, M.N., Aneeshkumar, V., Indu, G.K., Anilkumar, Y., Sajinkmar, K.S., 2018. Anatomy of impactites and shocked zircon grains from Dhala reveals Paleoproterozoic meteorite impact in the Archean basement rocks of Central India. Gondwana Research 54, 81–101.

Liu, Y.S., Gao, S., Hu, Z.C., Gao, C.G., Zong, K.Q., Wang, D.B., 2010. Continental and oceanic crust recycling-induced melt-peridotite interactions in the Trans-North China Orogen: U–Pb dating, Hf isotopes and trace elements in zircons of mantle xenoliths. Journal of Petrology 51, 537–571.

Oh, C.W., Kim, S.W., Choi, S.G., Zhai, M., Guo, J., Sajeev, K., 2005. First finding of eclogite facies metamorphic event in South Korea and its correlation with the Dabie–Sulu collision belt in China. The Journal of Geology 113, 226–232.

Oh, C.W., Rajesh, V.J., Seo, J., Choi, S.-G., Lee, J.H., 2010. Spinel compositions and tectonic relevance of the Bibong ultramafic bodies in the Hongseong collision belt, South Korea. Lithos 117, 198–208.

Oh, C.W., Seo, J., Choi, S.G., Rajesh, V.J., Lee, J.H., 2012. U–Pb SHRIMP zircon geochronology, petrogenesis, and tectonic setting of the Neoproterozoic Baekdong ultramafic rocks in the Hongseong collision belt, South Korea. Lithos 128–131, 100–112.

Park, S.-I., Kim, S.W., Kwon, S., Thanh, N.X., Yi, K., Santosh, M., 2014a. Paleozoic tectonics of the southwestern Gyeonggi massif, South Korea: insight from geochemistry, chromian-spinel chemistry and SHRIMP U–Pb geochronology. Gondwana Research 26, 684–698.

Park, S.-I., Kwon, S., Kim, S.W., Yi, K., Santosh, M., 2014b. Continental origin of the Bibong eclogite, southwestern Gyeonggi massif, South Korea. Journal of Asian Earth Sciences 95, 192–202.

Park, Y.S., Kim, S.W., Kee, W., Jeong, Y., Yi, K., Kim, J., 2009. Middle Jurassic tectonomagmatic evolution in the southwestern margin of the Gyeonggi Massif, South Korea. Geosciences Journal 13, 217–231.

Santosh, M., Hu, C.N., Kim, S.W., Tang, L., Kee, W.S., 2018. Late paleoproterozoic ultrahigh-temperature metamorphism in the Korean Peninsula. Precambrian Research 308, 111–125.

Seo, J., Choi, S.-G., Oh, C.W., Kim, S.W., Song, S.H., 2005. Genetic implications of two different ultramafic rocks from Hongseong area in the southwestern Gyeonggi Massif, South Korea. Gondwana Research 8, 539–552.

Seo, J., Oh, C.W., Choi, S.G., Rajesh, V.J., 2013. Two ultramafic rock types in the Hongseong area, South Korea: tectonic significance for northeast Asia. Lithos 175–176, 30–39.

Scherer, E., Munker, C., Mezger, K., 2001. Calibration of the lutetium–hafnium clock. Science 293, 683–687.

Shi, G., Cui, W., Cao, S., Jiang, N., Jian, P., Liu, D., Miao, L., Chu, B., 2008. Ion microprobe zircon U-Pb age and geochemistry of the Myanmar jadeitite. Journal of the Geological Society 165, 221–234.

Spencer, C.J., Yakymchuk, C., Ghaznavi, M., 2017. Visualising data distributions with kernel density estimation and reduced chi-squared statistic. Geoscience Frontiers 8, 1–6.

Sun, S.S., McDonough, W.F., 1989. Chemical and isotopic systematics of oceanic basalts: implications for mantle composition and processes. In: Saunders, A.D., Norry, M.J. (Eds.), Magmatism in Ocean Basins. Special Publication. Vol. 42. Geological Society of London, pp. 313–345.

Tsujimori, T., Liou, J.G., Wooden, J., Miyamoto, T., 2005. U-Pb dating of large zircons in low-temperature jadeitite from the Osayama serpentinite mélange, southwest Japan: insights into the timing of serpentinization. International Geology Review 47, 1048–1057.

Tsutsumi, Y., Yokoyama, K., Miyawaki, R., Matsubara, S., Terada, K., Hidaka, H., 2010. Ages of zircons in jadeitite and jadeite-bearing rocks of Japanese islands. Bulletin National Museum of Natural Sciences, Series C 36, 19–30.

Yang, Q.Y., Santosh, M., Maruyama, S., Nakagawa, M., 2016. Proto-Japan and tectonic erosion: evidence from zircon geochronology of blueschist and serpentinite. Lithosphere 8, 386–395.

Yang, F., Santosh, M., Tsunogae, T., Tang, L., Teng, X., 2017. Multiple magmatism in an evolving suprasubduction zone mantle wedge: the case of the composite mafic–ultramafic complex of Gaositai, North China Craton. Lithos 284–285, 525–544.

Yuan, H.L., Gao, S., Liu, X.M., Li, H.M., Gunther, D., Wu, F.Y., 2004. Accurate U–Pb age and trace element determinations of zircon by laser ablation–inductively coupled plasma mass spectrometry. Geostandards Newsletter 28, 353–370.